Transonic Turboprop Noise Prediction Using a Rotating Permeable-Surface FW-H Formulation in the Time Domain

# Transonic turboprop noise prediction using a rotating permeable-surface FW-H formulation in the time domain

E. Sticchi*and D. Ragni†and D. Casalino‡

Delft University of Technology, Flow Physics and Technology Department, Kluyverweg 1, 2629 HS Delft, Netherlands

F. Avallone§

Polytechnic University of Turin, Department of Mechanical and Aerospace Engineering, Corso Duca degli Abruzzi 24, Torino, 10129, Italy

**This work investigates the robustness of a transonic FW–H formulation for rotating permeable surfaces, developed to enable stable acoustic integration when the permeable surface moves at sonic conditions relative to the observer. The method, based on the de-singularized Formulations 1-DS and 1A-DS by Casalino, is assessed through comparison with classical FW–H approaches. Results show that the de-singularized formulation provides consistent far-field noise predictions, preserving high-frequency content by enabling the use of integration surfaces tightly fitted to the blade geometry. By comparison, the solid formulation underestimates acoustic levels due to the absence of quadrupole contributions, while the classical permeable formulation attenuates high-frequency content as a result of numerical dissipation when the integration surface is located away from the source region. A practical guideline is also provided for selecting the time-step ratio $\sigma$ between the FW–H and CFD time steps, whose value controls the balance between signal smoothing and maximum resolved frequency. Overall, the proposed formulation offers a robust and efficient approach for aeroacoustic predictions in transonic propeller applications.**

## I. Introduction

The ongoing development of advanced open-rotor configurations for next-generation aircraft, including innovative concepts employing swirl-recovery systems,[1] has renewed interest in predicting the aerodynamic noise generated by propellers and rotors operating in the transonic regime. In such conditions, blade tip Mach numbers approach unity, giving rise to shock formation and rapid variations of blade loading. These nonlinear flow features are responsible for the generation of high-speed impulsive (HSI) noise, which dominates the acoustic signature of many transonic rotors.[2] Accurate prediction of these mechanisms is essential both for reducing community noise during high-thrust operations and for mitigating cabin noise generated by nonlinear propagation and radiation effects in cruise conditions.[3]

In modern aeroacoustic practice, the prediction of aircraft noise from numerical flow simulations relies primarily on acoustic analogies. These approaches recast the nonlinear fluid-dynamic processes responsible

*PhD Candidate, Delft University of Technology, Faculty of Aerospace Engineering, Department of Flow Physics and Technology, Wind Energy Section, Aeroacoustics group, e.sticchi@tudelft.nl

†Associate Professor, Delft University of Technology, Faculty of Aerospace Engineering, Department of Flow Physics and Technology, Wind Energy Section, Aeroacoustics group, d.ragni@tudelft.nl, AIAA Member

‡Full Professor, Delft University of Technology, Faculty of Aerospace Engineering, Department of Flow Physics and Technology, Wind Energy Section, Aeroacoustics group, d.casalino@tudelft.nl

§Full Professor, Polytechnic University of Turin, Department of Mechanical and Aerospace Engineering, francesco.avallone@polito.it, AIAA Member

for sound generation into equivalent acoustic source terms. The resulting radiated field is then obtained by solving a wave equation governing the propagation of these equivalent sources into the far field through a uniform medium. Lighthill's acoustic analogy established the theoretical framework by deriving such a wave-like equation through an exact rearrangement of the Navier–Stokes equations, identifying turbulence as an effective quadrupole distribution responsible for sound generation.[4] Curle[5] extended this theory to include the effects of rigid surfaces, demonstrating how dipole sources arise from fluctuating aerodynamic loads on solid boundaries. For configurations involving bodies in arbitrary motion, the Ffowcs Williams–Hawkings (FW–H) equation extended these ideas to moving surfaces and volumetric turbulence sources, providing a formulation that reduces to the Lighthill and Curle analogies in appropriate limits.[6] Such an equation has served as the starting point for many time- and frequency-domain computational methods in aeroacoustics.

Time-domain implementations are commonly based on Farassat's Formulations 1 and 1A,[7] which analytically remove observer-time derivatives and have proven particularly effective for subsonic blade motion. When the flow over the blade reaches transonic conditions, however, nonlinear flow structures such as shocks and strong vortical disturbances extend away from the blade surface and act as additional acoustic sources. In these situations, the classical "solid-surface" FW–H formulation, which accounts only for thickness and loading contributions, may no longer provide an accurate representation of the acoustic field unless the nonlinear quadrupole sources are explicitly integrated over the surrounding flow volume.[8,9]

Direct evaluation of the quadrupole volume terms is rarely practical in realistic rotor simulations because of the large computational cost and the difficulty of storing the required flow-field information. A widely adopted alternative consists of evaluating the FW–H equation on a permeable surface enclosing the solid body and the surrounding nonlinear flow structures. This approach, originally introduced by Di Francescantonio,[10] allows the integration surface to be placed arbitrarily in the flow field while preserving the exactness of the complete FW-H formulation. In this case, the classical thickness and loading source terms are replaced by so-called pseudo-thickness and pseudo-loading contributions defined on the permeable surface. When the surface fully encloses the relevant nonlinear flow structures, the quadrupole volume contribution can be neglected without loss of accuracy.[8] The placement of the permeable integration surface is therefore a critical aspect of rotor-noise prediction. For transonic rotors operating without shock delocalization, it has been shown that a cylindrical surface tightly surrounding the blades can provide accurate predictions.[11] However, when shocks detach from the blade, they can extend beyond two chord lengths, requiring a substantial enlargement of the integration surface to enclose the relevant flow field.[12] In such situations, portions of the integration surface may move at sonic or supersonic radiative speed with respect to the observer, which introduces additional numerical challenges in the time-domain evaluation of the FW–H integrals.

The classical time-domain formulations of Farassat rely on the assumption that the radiative Mach number remains strictly subsonic. When the radiative Mach number approaches unity, as commonly occurs in transonic rotor flows or in the presence of shock-induced source motion, the standard time-domain evaluation exhibits singular behavior. This numerical difficulty severely limits the robustness of conventional time-domain FW–H implementations in the regimes where accurate prediction of HSI noise is most needed.

Several strategies have been proposed in the literature to address this limitation. One class of approaches is based on emission-surface concepts, in which the integration is reformulated in terms of emission time rather than observer time, thereby regularizing the multiple emission times associated with supersonic source motion.[12] These formulations provide a consistent geometrical description of the acoustic radiation process for supersonic sources. However, they require complex numerical procedures to identify and track multiple emission points and are therefore difficult to implement efficiently in large-scale rotor-noise simulations.

A different approach is represented by collapsing-sphere formulations, originally introduced by Farassat and later extended by Brentner and Farassat.[2,13,14] In these methods, the radiation process is interpreted geometrically through collapsing wavefront surfaces that avoid the singular behavior of the classical retarded-time kernels. While this approach provides valuable physical insight and can regularize certain singularities, it generally relies on simplified representations of the source distribution and is not easily applicable to complex three-dimensional CFD data for practical rotor configurations.

Another important line of development is represented by the fully non-compact integration techniques developed at ONERA.[15–17] In these approaches, each surface or volume element is treated as non-compact and its contribution is integrated directly in time, which avoids nonphysical Doppler singularities and makes it possible to perform the acoustic calculation directly from CFD data expressed in the rotating frame, even in the presence of supersonically moving emission points.[17] These methods have shown high robustness and have been successfully applied to transonic rotors and propellers. Their main limitation, however, is

that they rely on a dedicated integration framework that is more complex than the classical retarded-time implementation of Farassat's formulations, and they do not directly preserve the standard time-domain structure of Formulations 1 and 1A.

Although these approaches have demonstrated improved robustness in specific configurations, none has emerged as a universally accepted standard for predicting transonic rotor noise, particularly when shocks delocalize and complex nonlinear flow structures interact with the acoustic integration surface. As a consequence, the development of robust and efficient FW–H formulations capable of handling both subsonic and transonic regimes, while retaining the simplicity of classical time-domain implementations, remains an active area of research and continues to pose a formidable challenge for aeroacoustic specialists.

To address this challenge, the present work builds upon the recently proposed de-singularized formulation of the FW–H equation introduced by Casalino.[18] In this approach, the classical retarded-time formulation is modified to remove the singular behavior occurring when the radiative Mach number reaches sonic conditions. The resulting de-singularized formulations, referred to as Formulations 1-DS and 1A-DS, extend the applicability of the classical Farassat framework to permeable surfaces undergoing both subsonic and supersonic relative motion, while preserving the computational efficiency of time-domain FW–H implementations. This makes the formulation particularly attractive for practical rotor-noise prediction in transonic operating conditions.

The goal of the present paper is to investigate the robustness of this permeable-surface transonic FW–H formulation in the time domain for predicting the noise generated by a propeller operating in transonic axial-flow conditions. The assessment is carried out through a systematic comparison with classical FW–H formulations, with the aim of evaluating the ability of the de-singularized approach to provide consistent predictions of acoustic amplitude and spectral content in the presence of strong compressibility effects. Particular attention is devoted to the role of integration-surface placement and to the temporal sampling, leading to practical guidelines for the selection of the time-step ratio $\sigma$, defined as the ratio between the FW–H integration time step and the CFD time step.

The paper is outlined as follows. Section II describes the theoretical framework and introduces the de-singularized retarded-time FW–H formulation. The reference turboprop configuration and operating conditions are presented in Sec. III. The numerical setup used to perform PowerFLOW® simulations is described in Sec. IV. Results obtained using movable- and fixed-surface FW–H calculations are compared and discussed in Sec. V. Finally, the main conclusions are discussed in Sec. VI.

## II. FW-H Formulation

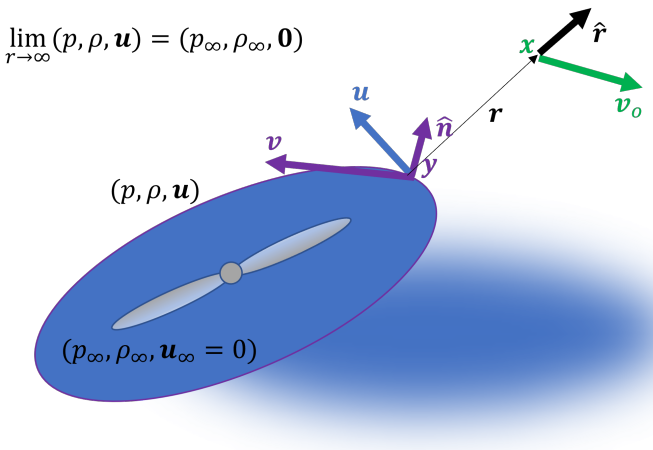


Figure 1: FW-H conceptual scheme.

Referring to Fig. 1, consider a control surface defined by $f(\mathbf{x},t)=0$, whose points move with velocity $\mathbf{v}(\mathbf{x},t)$. The surface $f=0$ is such that $\nabla f=\hat{\mathbf{n}}$, where $\hat{\mathbf{n}}$ represents the outward-pointing unit normal vector. This surface evolves with arbitrary motion and encloses a solid body, which itself moves arbitrarily within a fluid initially at rest. The presence of the body generates local flow disturbances, while at sufficiently large

distances the fluid returns to a quiescent condition.

A representative example is that of a helicopter rotor in forward flight, where the blades undergo cyclic pitching and are surrounded by permeable surfaces translating with the helicopter velocity and rotating with the rotor angular speed; however, for generality, cyclic pitching of these surfaces is not assumed here. The acoustic field produced by the unsteady flow is detected by an observer moving with velocity $\mathbf{v}_o$, which is taken to be constant for simplicity.

The case of a rotor operating in a wind tunnel with free-stream velocity $\mathbf{U}_\infty$ can be readily obtained by considering the rotor, the permeable surface, and the observer all translating at the constant velocity $-\mathbf{U}_\infty$. It is important to note that $\mathbf{u}$ denotes the absolute flow velocity; therefore, when the flow solution is obtained from a CFD simulation in wind-tunnel configuration, a Galilean transformation must be applied, namely $\mathbf{u} = \mathbf{u}_{\text{CFD}} - \mathbf{U}\infty$. Likewise, if the CFD computation is carried out in a rotating reference frame, the absolute velocity must be reconstructed.

Using generalized flow variables,[19] the flow field enclosed by the surface, i.e. $f<0$, can be replaced by a quiescent fluid and a surface distribution of sources which restore the conservative character of the field. Therefore, the generalized continuity and the linear momentum equations read:

$$\begin{aligned}
&\frac{\overline{\partial}}{\partial t}\left[(\rho-\rho_\infty)\ H(f)\right] + \frac{\overline{\partial}}{\partial x_i}\left[\rho\, u_i\, H(f)\right] = Q\,\delta(f) \quad \text{with}\\
&Q = \rho_\infty\, U_i\, \hat{n}_i \quad \text{and}\\
&U_i = \left(1-\frac{\rho}{\rho_\infty}\right) v_i + \frac{\rho\, u_i}{\rho_\infty}
\end{aligned} \tag{1}$$

and

$$\begin{aligned}
&\frac{\overline{\partial}}{\partial t}\left[\rho\, u_i\, H(f)\right] + \frac{\overline{\partial}}{\partial x_j}\left[(\rho\, u_i\, u_j + P_{ij})\ H(f)\right] = L_i\,\delta(f) \quad \text{with}\\
&L_i = P_{ij}\,\hat{n}_j + \rho\, u_i\,(u_n - v_n) \quad \text{and}\\
&P_{ij} = (p-p_\infty)\,\delta_{ij} - \tau_{ij},
\end{aligned} \tag{2}$$

where $Q\,\delta(f)$ and $L_i\,\delta(f)$ denote surface source distributions of mass and linear momentum, respectively. The field quantities $p$, $\rho$, and $\tau_{ij}$ are fluid pressure, density, and viscous stress tensor. The following generalized derivatives have been used in Eqs. (1) and (2):

$$\frac{\overline{\partial} H(f)}{\partial t} = \delta(f)\,\frac{\partial f}{\partial t} = -\delta(f)\, v_n \tag{3}$$

$$\frac{\overline{\partial} H(f)}{\partial x_i} = \delta(f)\,\frac{\partial f}{\partial x_i} = \delta(f)\,\hat{\mathbf{n}} \tag{4}$$

Far from the source region, the fluid can be considered at rest and Eqs. (1) and (2) can be combined to obtain a standard wave equation describing the propagation of an acoustic disturbance $p' = p - p_\infty$ in a quiescent medium, i.e.

$$\Box^2 p' \equiv \left(\frac{1}{c_\infty^2}\frac{\partial^2}{\partial t^2} - \nabla^2\right) p' = 0, \tag{5}$$

where $c_\infty$ is the sound speed in the quiescent medium. Instead, if the flow perturbations are included, Eqs. (1) and (2) can be arranged into the FW-H equation where the flow perturbations appear as source terms of the wave equation. More precisely, by subtracting the divergence of Eq. (2) to the time derivative of Eq. (1), the following differential form of the FW-H equation can be obtained:

$$\Box^2\left\{(\rho-\rho_\infty)\, c_\infty^2\, H(f)\right\} = \frac{\partial^2}{\partial x_i \partial x_j}\left\{T_{ij}\, H(f)\right\} - \frac{\partial}{\partial x_i}\left\{L_i\,\delta(f)\right\} + \frac{\partial}{\partial t}\left\{Q\,\delta(f)\right\}, \tag{6}$$

where

$$T_{ij} = \rho\ u_i u_j + \left(p' - c_\infty^2\,\rho'\right)\delta_{ij} - \tau_{ij} \tag{7}$$

is the well-known Lighthill's stress tensor. If the density perturbations are small, as usually happens at the observation distances, the term $(\rho-\rho_\infty)\,c^2$ can be replaced by $p'$ and Eq. (6) can be interpreted as an inhomogeneous wave equation for the acoustic pressure.

In aeroacoustic theory, the three source terms appearing on the right-hand side of Eq. (6) are commonly referred to as the quadrupole, (pseudo-)loading, and (pseudo-)thickness contributions, respectively. The loading and thickness contributions are distributed over a surface, as indicated by $\delta(f)$. When the control surface coincides with an actual solid boundary, the thickness term represents the fluid displacement caused by the body motion, whereas the loading term accounts for the unsteady forces exerted by the body on the surrounding fluid.

By contrast, the quadrupole term is distributed throughout a volume, as denoted by $H(f)$, and represents flow nonlinearities ($u_i u_j$) as well as entropy-related effects ($p'-c^2\rho'$) in the region outside the control surface. These include, for example, turbulent fluctuations and shock waves generated by the motion of the body through the fluid.

In what follows, the integration surface is assumed to be sufficiently extended to enclose all source mechanisms associated with turbulence, shock waves, and entropy variations, so that the volume contribution can be neglected. However, if the surface intersects strongly turbulent regions, such as a jet shear layer or a rotor wake, neglecting the volume term may lead to an imbalance in the FW–H analogy and the appearance of spurious acoustic radiation. In such cases, these non-physical effects can be alleviated by introducing additional surface source terms that approximate the contribution of the omitted volume sources.[20–22]

### II.A. Integral solutions of the FW-H equation

Following Farassat,[7] a formal integral solution of the non-homogeneous wave equation $\Box^2 p'(\mathbf{x},t) = Q(\mathbf{x},t)\,\delta(f)$ can be obtained by convoluting the right-hand-side with the free-space Green's function $G(\mathbf{x},t;\mathbf{y},\tau) = \delta(g)\,/\,(4\pi r)$, where $g = \tau - t + r/c_\infty$ and $r = |\mathbf{x}-\mathbf{y}|$. Here $(\mathbf{x},t)$ and $(\mathbf{y},\tau)$ are the observer and the source space-time variables, respectively. The solution reads:

$$4\pi p'(\mathbf{x},t) = \int_{-\infty}^{t} \iiint_{\mathbb{R}^3} Q(\mathbf{y},\tau)\,\delta(f)\,\frac{\delta(g)}{r}\,\mathrm{d}\mathbf{y}\,\mathrm{d}\tau. \tag{8}$$

By introducing a body-fixed reference frame, a point of the moving integration surface is defined by $\mathbf{y} = \mathbf{y}(\eta,\tau)$, where $\eta$ is the time-independent position of the point in the body-fixed reference frame. Thus, setting $\hat{Q}(\eta,\tau) = Q(\mathbf{y}(\eta),\tau)$ and $\hat{f}(\eta,\tau) = f(\mathbf{y}(\eta),\tau)$, and performing a change of variable $\mathbf{y} \to \eta$, Eq. (8) becomes:

$$4\pi p'(\mathbf{x},t) = \int_{-\infty}^{t} \iiint_{\mathbb{R}^3} \hat{Q}(\eta,\tau)\,\delta\Big(\hat{f}\Big)\,\frac{\delta(g)}{r}\,\mathrm{d}\eta\,\mathrm{d}\tau. \tag{9}$$

In order to perform the time integration, a transformation of variable $\tau \to g$ can be applied, leading to:

$$4\pi p'(\mathbf{x},t) = \int \iiint_{\mathbb{R}^3} \hat{Q}(\eta,\tau)\,\delta\Big(\hat{f}\Big)\,\frac{\delta(g)}{r\,|\partial g/\partial\tau|}\,\mathrm{d}\eta\,\mathrm{d}g. \tag{10}$$

Then, knowing that $\partial g/\partial\tau = 1 - v_i\hat{r}_i/c_\infty = 1 - M_r$, and by using the properties of the Dirac function $\delta(g)$, Eq. (10) becomes:

$$4\pi p'(\mathbf{x},t) = \iiint_{\mathbb{R}^3} \left\{ \frac{\hat{Q}(\eta,\tau)}{r\,|1-M_r|}\,\delta\Big(\hat{f}\Big) \right\}_{g=0} \mathrm{d}\eta, \tag{11}$$

where evaluation of the integrand at $g = 0$ means at the so-called retarder or emission time $\tau_e$, solution of the retarded time equation:

$$g = \tau_e - t + \frac{|\mathbf{x}(t) - \mathbf{y}(\eta,\tau_e)|}{c_\infty} = 0. \tag{12}$$

Finally, by using the property of the Dirac function $\delta(f)$, the so-called retarded-time solution of the wave equation reads:

$$4\pi p'(\mathbf{x},t) = \int_{\hat{f}=0} \frac{\hat{Q}(\eta,\tau_e)}{r_e\,|1-M_{r\,e}|}\,\mathrm{d}S_\eta, \tag{13}$$

where $r_e$ is the source-to-observer distance at the emission time and $M_{r\,e}$ is the surface velocity Mach number projected in the source-to-observer direction at the emission time.

Equation (13) can be now used to obtain an integral solution of Eq. (6). Restricting to the pseudo-thickness and pseudo-loading terms, the solution reads:

$$4\pi p'(\mathbf{x},t) = 4\pi p'_T(\mathbf{x},t) + 4\pi p'_L(\mathbf{x},t) \equiv \frac{\partial}{\partial t}\int\limits_{\hat{f}=0} \frac{\rho_\infty \hat{U}_n(\eta,\tau_e)}{r_e\,|1-M_{r\,e}|}\,\mathrm{d}S_\eta - \frac{\partial}{\partial x_i}\int\limits_{\hat{f}=0} \frac{\hat{L}_i(\eta,\tau_e)}{r_e\,|1-M_{r\,e}|}\,\mathrm{d}S_\eta. \tag{14}$$

By making use of the following identity:

$$\frac{\partial}{\partial x_i}\left(\frac{\delta(g)}{r}\right) = -\frac{1}{c_\infty}\frac{\partial}{\partial t}\left(\frac{\hat{r}_i\delta(g)}{r}\right) - \frac{\hat{r}_i\delta(g)}{r^2}, \tag{15}$$

Eq. (14) becomes:

$$4\pi p'(\mathbf{x},t) = \rho_\infty \frac{\partial}{\partial t}\int\limits_{\hat{f}=0} \frac{\hat{U}_n(\eta,\tau_e)}{r_e\,|1-M_{r\,e}|}\,\mathrm{d}S_\eta + \frac{1}{c_\infty}\frac{\partial}{\partial t}\int\limits_{\hat{f}=0} \frac{\hat{L}_r(\eta,\tau_e)}{r_e\,|1-M_{r\,e}|}\,\mathrm{d}S_\eta + \int\limits_{\hat{f}=0} \frac{\hat{L}_r(\eta,\tau_e)}{r_e^2\,|1-M_{r\,e}|}\,\mathrm{d}S_\eta, \tag{16}$$

where the subscripts $n$ and $r$ denote projection along the surface normal $\hat{\mathbf{n}}$ and radiation direction $\hat{\mathbf{r}}$, respectively. Equation (16) is a permeable-surface generalization of Farassat retarder-time *Formulation 1* derived for the first time in 1975 for a solid integration surface.[2]

It is important to point out that Equation (16) remains valid for a moving observer, as the retarded-time equation is solved for any instantaneous observer position. However, the partial time derivative on the right-hand side must be evaluated at a fixed observer location $\mathbf{x}$. Further details on the formulation, along with a discussion of the treatment of a moving observer, can be found in Ref.[18]

Following Farassat,[7] an alternative solution of Eq. (6) can be obtained by converting the time derivative at a fixed observer into an emission time derivative using the following equivalence:

$$\left.\frac{\partial}{\partial t}\right|_{\mathbf{x}} = \left[\frac{1}{1-M_r}\frac{\partial}{\partial \tau}\right]_e \tag{17}$$

together with the following expressions:

$$\frac{\partial r}{\partial \tau} = -c_\infty\, M_r \tag{18}$$

$$\frac{\partial \hat{r}_i}{\partial \tau} = \frac{\hat{r}_i\, c_\infty\, M_r - c_\infty\, M_i}{r} \tag{19}$$

$$\frac{\partial M_r}{\partial \tau} = \frac{1}{r}\left\{ r\,\hat{r}_i\,\frac{\partial M_i}{\partial \tau} + c_\infty\,\left(M_r^2 - M^2\right)\right\} \tag{20}$$

In Eq. (17), the symbol $|_{\mathbf{x}}$ indicates derivatives taken at a fixed observer position, while the subscript $e$ indicates evaluation at the emission time. This leads to the well-known *Formulation 1A* published for the first time by Farassat & Succi in 1980:[23]

$$4\pi\, p'_T(\mathbf{x},t) = \int\limits_{f=0}\left[\frac{\rho_\infty\left(\dot{U}_n + U_{\dot{n}}\right)}{r\,(1-M_r)^2}\right]_e \mathrm{d}S_\eta + \int\limits_{f=0}\left[\frac{\rho_\infty U_n\left(r\dot{M}_r + c_\infty\left(M_r - M^2\right)\right)}{r^2\,(1-M_r)^3}\right]_e \tag{21}$$

$$\begin{aligned} 4\pi\, p'_L(\mathbf{x},t) = {} & \frac{1}{c_\infty}\int\limits_{f=0}\left[\frac{\dot{L}_r}{r\,(1-M_r)^2}\right]_e \mathrm{d}S_\eta + \int\limits_{f=0}\left[\frac{L_r - L_M}{r^2\,(1-M_r)^2}\right]_e \mathrm{d}S_\eta \\ & + \frac{1}{c_\infty}\int\limits_{f=0}\left[\frac{L_r\left(r\dot{M}_r + c_\infty\left(M_r - M^2\right)\right)}{r^2\,(1-M_r)^3}\right]_e \mathrm{d}S_\eta, \end{aligned} \tag{22}$$

where $\mathbf{M}$ is the Mach number vector of a source point on the integration surface, and the remaining terms are defined as:

$$\begin{aligned} &U_n = U_i\,\hat{n}_i \qquad U_{\dot{n}} = U_i\,\dot{\hat{n}}_i \qquad \dot{U}_n = \dot{U}_i\,\hat{n}_i \\ &M_r = M_i\,\hat{r}_i \qquad \dot{M}_r = \dot{M}_i\,\hat{r}_i \\ &L_r = L_i\,\hat{r}_i \qquad \dot{L}_r = \dot{L}_i\,\hat{r}_i \qquad L_M = L_i\,M_i \end{aligned} \tag{23}$$

In the above equations, dots on quantities denote time derivatives with respect to the source time $\tau$. Notice that we have removed the absolute value of the Doppler amplification factor since we are implicitly assuming that Formulation 1A is used only for parts of the moving surface in radiative subsonic motion ($M_r<1$).

### II.B. Treatment of the transonic singularity

Both Formulation 1 and 1A are affected by the so-called transonic singularity occurring at unitary value of the radiative Mach number $M_r$. The retarded-time integral solutions can be solved using an advanced-time algorithm consisting in using the retarded-time equation to determine the reception time at a given source emission time.[18,24] Let's therefore rewrite Eq. (12) as:

$$t = \tau_e + \frac{|\mathbf{x}(t) - \mathbf{y}(\eta, \tau_e)|}{c_\infty}, \tag{24}$$

from which can derive the derivative of the reception time with respect to the emission time:

$$\frac{\mathrm{d}t}{\mathrm{d}\tau_e} = 1 + \frac{\mathbf{x}(t) - \mathbf{y}(\eta, \tau_e)}{c_\infty \, |\mathbf{x}(t) - \mathbf{y}(\eta, \tau_e)|} \cdot \left( \frac{\mathrm{d}\mathbf{x}}{\mathrm{d}t} \frac{\mathrm{d}t}{\mathrm{d}\tau_e} - \frac{\mathrm{d}\mathbf{y}}{\mathrm{d}\tau_e} \right) = 1 + M^o_{r\,e} \frac{\mathrm{d}t}{\mathrm{d}\tau_e} - M_{r\,e} = \frac{1 - M_{r\,e}}{1 - M^o_{r\,e}}, \tag{25}$$

where $M^o_{r\,e}$ is the observer Mach number projected on the radiation direction at the emission time. Notice that, for an *observer moving at constant arbitrary subsonic speed* ($M^o_{r\,e}<1$), the advanced time equation has a unique solution, which means that, for a given emission time, there exists a unique value of the reception time. This is not the case of the retarded-time equation Eq. (12) that may have up to three distinct solutions for transonic rotors. In that case, the formal solution Eq. (11) is to be intended by a summation over the distinct roots of $g=0$. Such a complication is removed by adopting an advanced-time algorithm. Also notice that the sign of $\mathrm{d}t/\,\mathrm{d}\tau_e$ indicates that, for $M_r>1$, signals emitted later are received earlier. If we want to preserve the physical positive meaning of an incremental time-step in the integral evaluation, then we can simply assume:

$$\frac{\mathrm{d}t}{\mathrm{d}\tau_e} = \frac{|1 - M_{r\,e}|}{1 - M^o_{r\,e}}. \tag{26}$$

Interestingly, for $M_{r\,e} \to 1$ and a finite emission time increment, the reception time increment vanishes, meaning that the infinite infinitesimal wave perturbations emitted at a given time reach the observer all at the same time. The sum of all these infinitesimal perturbations is necessarily finite, thus revealing the mathematical and not physical nature of the singularity in Eqs. (16), (21) and (22). Following Ref.,[18] the pressure measured by an observer during a discrete time interval $i$ can be evaluated as the integral mean of the signal over that interval:

$$P(\mathbf{x}, t_i) = \frac{1}{\Delta t} \int_{(i-1/2)\Delta t}^{(i+1/2)\Delta t} p(\mathbf{x}, t) \, \mathrm{d}t = \frac{1}{\Delta t} \int_{(i-1/2)\Delta t}^{(i+1/2)\Delta t} p(\mathbf{x}, t) \left( \frac{\mathrm{d}t}{\mathrm{d}\tau_e} \right) \mathrm{d}\tau_e = \frac{1}{\Delta t} \int_{(i-1/2)\Delta t}^{(i+1/2)\Delta t} p(\mathbf{x}, t) \, \frac{|1 - M_{r\,e}|}{1 - M^o_{r\,e}} \, \mathrm{d}\tau_e, \tag{27}$$

where the integrals in the emission time $\tau_e$ must be interpreted as summation of all contributions with reception time in the interval $[i-1/2, i+1/2]\,\Delta t$. Interestingly, the integral averaging process has the effect of reducing the order of the singularity. Therefore, taking advantage of the linearity of the wave operator,

we can restate Formulation 1 in the following De-Singularized (DS) form:

$$q^T(\mathbf{x},t) = \rho_\infty \int\limits_{\hat{f}=0} \frac{\hat{U}_n(\eta,\tau_e)}{r_e\,|1-M_{re}|}\,\mathrm{d}S_\eta, \quad q^L(\mathbf{x},t) = \frac{1}{c_\infty}\int\limits_{\hat{f}=0} \frac{\hat{L}_r(\eta,\tau_e)}{r_e\,|1-M_{re}|}\,\mathrm{d}S_\eta, \tag{28}$$

$$p^L(\mathbf{x},t) = \int\limits_{\hat{f}=0} \frac{\hat{L}_r(\eta,\tau_e)}{r_e^2\,|1-M_{re}|}\,\mathrm{d}S_\eta \tag{29}$$

$$\mathcal{Q}^T(\mathbf{x},t_i) = \frac{1}{\Delta t}\int\limits_{(i-1/2)\Delta t}^{(i+1/2)\Delta t} q^T(\mathbf{x},t)\,\frac{|1-M_{re}|}{(1-M_{re}^o)^2}\,\mathrm{d}\tau_e \simeq \frac{1}{\sigma}\sum_{(i-1/2)\Delta t}^{(i+1/2)\Delta t}\int\limits_{\hat{f}=0} \frac{\rho_\infty \hat{U}_n(\eta,\tau_e)}{r_e\,(1-M_{re}^o)^2}\,\mathrm{d}S_\eta \tag{30}$$

$$\mathcal{Q}^L(\mathbf{x},t_i) = \frac{1}{\Delta t}\int\limits_{(i-1/2)\Delta t}^{(i+1/2)\Delta t} q^L(\mathbf{x},t)\,\frac{|1-M_{re}|}{(1-M_{re}^o)^2}\,\mathrm{d}\tau_e \simeq \frac{1}{\sigma}\sum_{(i-1/2)\Delta t}^{(i+1/2)\Delta t}\int\limits_{\hat{f}=0} \frac{\hat{L}_r(\eta,\tau_e)/c_\infty}{r_e\,(1-M_{re}^o)^2}\,\mathrm{d}S_\eta \tag{31}$$

$$\mathcal{P}^L(\mathbf{x},t_i) = \frac{1}{\Delta t}\int\limits_{(i-1/2)\Delta t}^{(i+1/2)\Delta t} p^L(\mathbf{x},t)\,\frac{|1-M_{re}|}{1-M_{re}^o}\,\mathrm{d}\tau_e \simeq \frac{1}{\sigma}\sum_{(i-1/2)\Delta t}^{(i+1/2)\Delta t}\int\limits_{\hat{f}=0} \frac{\hat{L}_r(\eta,\tau_e)}{r_e^2\,(1-M_{re}^o)}\,\mathrm{d}S_\eta \tag{32}$$

$$4\pi\,P(\mathbf{x},t_i) = 4\pi\,P^T(\mathbf{x},t_i) + 4\pi\,P^L(\mathbf{x},t_i) = \frac{\partial \mathcal{Q}^T}{\partial t}(\mathbf{x},t_i) + \frac{\partial \mathcal{Q}^L}{\partial t}(\mathbf{x},t_i) + \mathcal{P}^L(\mathbf{x},t_i)\,, \tag{33}$$

where the additional $1-M_{re}^o$ Doppler factor in Eqs. (30) and (31) accounts for the effect of the fixed-observer time derivative. Equation (33) is the final expression of the de-singularized thickness and loading noise contributions of the *Formulation 1-DS* proposed by Casalino.[18] The unsteady integral contributions $\mathcal{Q}^T$ and $\mathcal{Q}^L$ are derived numerically by using an equally-spaced series of values at discrete time $t_i$. Notice that in this advanced-time framework, the emission time is to be interpreted as the constant time step of the CFD solution sampling ($\tau_e \equiv t_{\mathrm{CFD}}$). In order to guarantee sufficient smoothness of the final noise signals, the reception time step $\Delta t$ must be sufficiently large compared to the CFD time step. Thus, introducing the time step ratio $\sigma = \Delta t/\Delta t_{\mathrm{CFD}}$, we must guarantee $\sigma > 1$ as a necessary condition for the smoothness of the computed noise signals.

Analogously, Casalino[18] obtained the *Formulation 1A-DS* of the thickness and loading noise contributions that:

$$\begin{aligned} 4\pi\,P^T(\mathbf{x},t_i) \simeq\ & \frac{1}{\sigma}\sum_{(i-1/2)\Delta t}^{(i+1/2)\Delta t}\int\limits_{f=0} \left[\frac{\rho_\infty\left(\dot{U}_n + U_{\dot{n}}\right)}{r\,(1-M_r)\,(1-M_{re}^o)}\right]_e \mathrm{d}S_\eta \\ & + \frac{1}{\sigma}\sum_{(i-1/2)\Delta t}^{(i+1/2)\Delta t}\int\limits_{f=0} \left[\frac{\rho_\infty\,U_n\left(r\dot{M}_r + c_\infty\left(M_r - M^2\right)\right)}{r^2\,(1-M_r)^2\,(1-M_{re}^o)}\right]_e \mathrm{d}S_\eta \end{aligned} \tag{34}$$

$$\begin{aligned} 4\pi\,P^L(\mathbf{x},t_i) \simeq\ & \frac{1}{\sigma}\sum_{(i-1/2)\Delta t}^{(i+1/2)\Delta t}\int\limits_{f=0} \left[\frac{\dot{L}_r}{c_\infty\,r\,(1-M_r)\,(1-M_{re}^o)}\right]_e \mathrm{d}S_\eta \\ & + \frac{1}{\sigma}\sum_{(i-1/2)\Delta t}^{(i+1/2)\Delta t}\int\limits_{f=0} \left[\frac{L_r - L_M}{r^2\,(1-M_r)\,(1-M_{re}^o)}\right]_e \mathrm{d}S_\eta \\ & + \frac{1}{\sigma}\sum_{(i-1/2)\Delta t}^{(i+1/2)\Delta t}\int\limits_{f=0} \left[\frac{L_r\left(r\dot{M}_r + c_\infty\left(M_r - M^2\right)\right)}{c_\infty\,r^2\,(1-M_r)^2\,(1-M_{re}^o)}\right]_e \mathrm{d}S_\eta. \end{aligned} \tag{35}$$

In the present work, both Formulation 1-DS and 1A-DS are applied concurrently within the FW–H integration procedure. Prior to the acoustic integration, surface elements that experience, at least once during the

simulation, a quasi-singular condition $|1 - M_{r,e}| < \epsilon$ are identified and tagged as singular. These elements are treated using Formulation 1-DS, while all remaining elements are evaluated using Formulation 1A-DS, which provides a more efficient yet consistent calculation in non-singular regions. This a priori classification, performed over the entire simulation time, avoids temporal switching and ensures robustness of the acoustic prediction. For further details on the algorithmic implementation of Eqs. (33) to (35), the reader is referred to Ref.[18] The present work makes use of the implementation available in *Opty∂B*-PFNOISESCAN 2026-GA.

A final remark is made for what concerns the parameters $\epsilon$, which defines the threshold for identifying quasi-singular conditions, and $\sigma$, defined as the ratio between the FW–H integration time step $\Delta t$ and the CFD time step $\Delta t_{\mathrm{CFD}}$. Thanks to the consistency between Formulations 1-DS and 1A-DS, the acoustic results exhibit limited sensitivity to the specific value of $\epsilon$.[18] The parameter $\sigma$, instead, directly determines the temporal resolution of the acoustic signal. In particular, increasing $\sigma$ results in a smoother signal but reduces the maximum resolvable frequency, as the time integration effectively introduces a low-pass filtering effect. To avoid aliasing and ensure accurate reconstruction of the acoustic spectrum up to a target maximum frequency $f_{\max}$, the integration time step must satisfy the Nyquist criterion, which can be written as:

$$\Delta t = \sigma \Delta t_{\mathrm{CFD}} \leq \frac{1}{N_{\mathrm{Nyq}} f_{\max}}, \tag{36}$$

where $N_{\mathrm{Nyq}} \geq 2$ is a user-defined safety factor accounting for practical deviations from the ideal Nyquist limit. In practice, values of $\sigma \approx 8$–$10$ are found to provide sufficient smoothing while retaining the relevant frequency content. Accordingly, the CFD time step can be selected as $\Delta t_{\mathrm{CFD}} = 1/(\sigma N_{\mathrm{Nyq}} f_{\max})$ to ensure consistency between temporal resolution and spectral accuracy.

## III. Turboprop configuration

The configuration analyzed in this study consists of the six-bladed propeller, previously adopted in Ref.[25] as the propulsive unit of the Clean Aviation HERWINGT strut-braced wing aircraft configuration. The propeller geometry is characterized by a disk diameter of 4.50 m and a hub-to-diameter ratio of 0.22.

The rotational speed is fixed at 1050 RPM, consistent with the nominal cruise condition of the HERWINGT design mission. The collective pitch angle is trimmed to provide a thrust of around 0.005. The simulation reproduces cruise flight at $M_\infty = 0.50$ ($U_\infty \approx 154$ m/s) and altitude $h = 25{,}000$ ft, for which the ambient static pressure and temperature are $p_\infty = 37{,}601$ Pa and $T_\infty = 238.6$ K, respectively. Under these conditions, the propeller operates in transonic regime, with a local tip Mach number of approximately 0.95.

Figure 2 illustrates the propeller configuration. Figure 2(a) shows the propeller geometry in the xz plane, while Fig. 2(b) reports the radial distributions of blade chord and twist. The computational model includes the spinner to ensure a realistic representation of the aerodynamic loading and root-vortex formation in the near-hub region. The hub is elongated in the streamwise direction to mitigate blunt-body separation at its end, which would otherwise contaminate the near-wake development. No nacelle, pylon, or additional aircraft components are included, as they are not relevant to the objective of the paper.

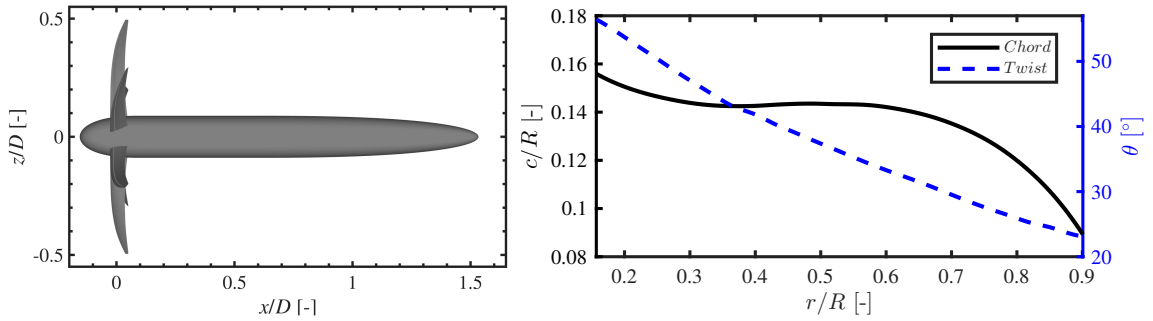


Figure 2: (a) Propeller geometry in the xz plane. (b) Chord and twist angle radial distribution of the propeller blades.

# IV. LBM/VLES numerical setup

## IV.A. Flow solver

The unsteady aerodynamic field is computed using the Lattice–Boltzmann Very Large Eddy Simulation (LBM/VLES) approach implemented in PowerFLOW® 6-2025-R2 by 3DS Dassault Systèmes. Compared to standard second-order Navier-Stokes finite-volume solvers, the LBM demonstrated to have lower dispersion and dissipation, making it particularly suited for aeroacoustic simulations.[26] The software used has been extensively used to accurately predict noise generated in complex flow problems, including full-vehicle configurations,[3,27–32] and propulsion systems.[33–36] A brief description of the solver is provided below.

In the LBM, the instantaneous state of the fluid flow is described at the mesoscopic level using distribution functions. Let $f(\mathbf{x}, t, \mathbf{V})$ be the non-normalized probability distribution function, representing the likelihood of finding a number of fluid particles moving with speed around $\mathbf{V}$ in the infinitesimal volume around the point $\mathbf{x}$ and around the time $t$. The evolution of $f$ in the phase space is described by the Boltzmann transport equation, which, in the absence of body forces, writes as

$$\frac{\partial f}{\partial t} + \mathbf{V} \cdot \boldsymbol{\nabla} f = C. \tag{37}$$

The LHS of Eq. (37) represents the advection of fluid particles, while the term $C$ on the RHS is used to model their collision. Discretizing Eq. (37) in space, time and velocity, using a Cartesian grid (i.e., lattice) and a predetermined number of discrete velocities, we obtain the lattice Boltzmann equation:

$$f_i(\mathbf{x} + \mathbf{V_i}\Delta t, t + \Delta t) - f_i(\mathbf{x}, t) = C_i(\mathbf{x}, t)\,\Delta t, \tag{38}$$

where $f_i$, $V_i$, and $C_i$ are the particle distribution function, the discrete particle velocity, and the collision operator along the $i^{th}$ lattice direction.

In PowerFLOW®, the velocity space discretization depends on the Mach number regime. In the present work, all simulations are performed using the fully transonic (TS) solver. In contrast to the standard low-Mach formulation based on 19 discrete velocities (D3Q19 model), the TS solver employs an extended velocity discretization corresponding to a multilayer lattice (D3Q33). This lattice provides sixth-order isotropy and enables accurate recovery of third-order hydrodynamic moments required for compressible and thermally coupled flows.[37] As a result, the method can operate reliably in the high-subsonic and transonic regimes, where compressibility effects become significant. A filtered collision operator[38] is employed to preserve Galilean invariance and eliminate unsupported non-hydrodynamic moments, ensuring solver stability and accuracy at elevated Mach numbers. In addition, a scalar transport equation for the total energy is solved to ensure exact energy conservation and thermodynamic consistency across the flow domain. Unlike the hybrid high-subsonic/transonic (HS/TS) formulation, no coupling between different lattice models is employed in the present simulations.

The solver employs a cubic lattice discretization composed of voxels with locally adaptive resolution, where adjacent regions differ by a factor of two in voxel size. Wall boundaries are treated using a volumetric formulation with specular reflection for slip and bounce-back for no-slip conditions. To reduce the computational cost of resolving the near-wall region, a pressure-gradient-corrected law-of-the-wall, extended to the buffer and viscous sub-layers, is applied at the first voxel adjacent to the surface.[39] A Very Large Eddy Simulation turbulence model is used to approximate the effect of the unresolved scale. In this approach, the molecular relaxation time is replaced by an effective turbulent relaxation time obtained from a renormalization-group (RNG) $k$–$\epsilon$ model. The formulation includes a swirl-correction term that dynamically adapts the model to the local vorticity and strain-rate fields, allowing the method to capture large-scale unsteadiness without explicit dependence on grid size. Moreover, unlike classical $\kappa$-$\epsilon$ models, the turbulence modelling is not used to compute an equivalent eddy viscosity. Instead, the quantities $\kappa$ and $\epsilon$ are used to recalibrate the Boltzmann model to the characteristic time scales of a turbulent flow motion by modifying the molecular relaxation time. As demonstrated by Chen et al.,[40,41] this results in a higher-order representation of the computed Reynolds stresses.

After solving Eq. (38), the macroscopic flow quantities can be obtained as follows:

$$\rho(\mathbf{x}, t) = \sum_i f_i(\mathbf{x}, t), \quad \rho\mathbf{u}(\mathbf{x}, t) = \sum_i \mathbf{V_i} f_i(\mathbf{x}, t). \tag{39}$$

### IV.B. Setup

The CFD simulation reproduces axial flow conditions characterised by a freestream Mach number of 0.50, a static pressure of 37.6 kPa, and an ambient temperature of 238.6 K. The computational domain encompasses the flow field around the isolated propeller and is bounded by a spherical far-field surface located at a radius of approximately 300 propeller diameters. Freestream conditions are imposed on this outer boundary.

The grid is composed of 16 voxel-resolution regions (VR0–VR15), where each successive level refines the spatial resolution by a factor of two. The finest voxel size, $6.90 \cdot 10^{-4}$ m, is applied in the vicinity of the solid surfaces. A grid convergence study is reported in Appendix .A, showing convergence of both aerodynamic loads and acoustic predictions for integration surfaces located close to the blade. A sliding-mesh local reference frame (LRF) encloses the propeller and spinner, rotating at 1050 RPM relative to the stationary background domain. No-slip boundary conditions are imposed on all solid surfaces, and boundary-layer trips are applied on the blades to model laminar–turbulent transition. To suppress spurious reflections, a sponge layer is introduced beyond 10 propeller diameters.

The voxel-resolution distribution, the outline of the fixed FW–H surface, and the LRF are illustrated in Fig. 3. The moving FW–H surface, employed for aeroacoustic calculations with the transonic formulation, is shown in Fig. 4 together with the pressure distribution in the rotor plane. The surface is constructed by combining an offset surface from the blade geometry in the inner region with a spherical cap near the blade tip, resulting in a smooth continuous integration surface. This definition allows the surface to remain as close as possible to the blade while enclosing the dominant nonlinear flow features associated with shock formation and delocalization. This surface can be interpreted as a compromise between the tight cylindrical surfaces used by Morgans and Dowling,[11] which are well suited for non-delocalized conditions, and the more extended helicoidal surfaces commonly adopted in transonic rotor-noise studies.[14,16,42] The proposed construction retains accuracy in the presence of shock delocalization while remaining simple to define and suitable for automated generation within propeller–airframe noise prediction workflows.

After an initial transient of two propeller revolutions, density, pressure, and velocity fields are sampled on the permeable surfaces, while pressure is sampled on the blade surface for the solid formulation. Data are then collected over ten additional revolutions. The sampling frequency is selected based on the spatial resolution of each integration surface and the requirements of the corresponding FW–H formulation. For the solid and rotating permeable surfaces, the sampling frequency is chosen to accurately reconstruct the acoustic signal up to the $20^{\text{th}}$ harmonic of the blade-passing frequency, consistent with the local grid resolution (approximately 15 voxels/timesteps per wavelength). In contrast, for the fixed permeable surface, a lower sampling frequency (6.6 kHz) is adopted, reflecting both the coarser spatial resolution away from the blade and the attenuation of high-frequency fluctuations due to numerical dissipation. As discussed in Sec. V and further analysed in Appendix .A, this limits the effective frequency range of the acoustic signal captured with this formulation. For the moving permeable surface, the sampling frequency is increased to satisfy the requirements of the de-singularized FW–H formulation. In particular, a time-step ratio $\sigma = 10$ is adopted (as discussed in Sec. II.B), implying a temporal resolution ten times higher than that of a standard permeable formulation for a given maximum frequency of interest (65.9 kHz). This ensures consistency between temporal resolution and spectral accuracy for the transonic formulation.

Formulation Farassat 1-A is used for solid and fixed FW-H surface, while the formulations 1A-DS and 1-DS are used for the moving FW-H surface. For comparison with the fixed FW–H surface, phase-shifted copies of the signal obtained from the moving FW–H surface are combined to reconstruct the contribution of all blades, assuming periodic rotor operation and uniform blade spacing. The computational cost of the FW–H post-processing and the associated data storage requirements depend on the formulation and sampling strategy. In the present work, the size of the sampled datasets is approximately 136 GB for the solid formulation, 132 GB for the fixed permeable formulation, and 147 GB for the rotating permeable formulation. The corresponding post-processing costs are all of the same order of $10^3$ CPU hours for 180 microphones. Observers are located on an arc in the rotor transversal plane at a distance of 15 m ($\approx$ 3 propeller radii).

## V. Results

The results are presented as follows. First, the dilatation field obtained directly from the CFD solution is analysed to identify the main acoustic source mechanisms. Then, the far-field radiation is assessed through directivity plots, followed by a comparison of the frequency spectra at a representative observer

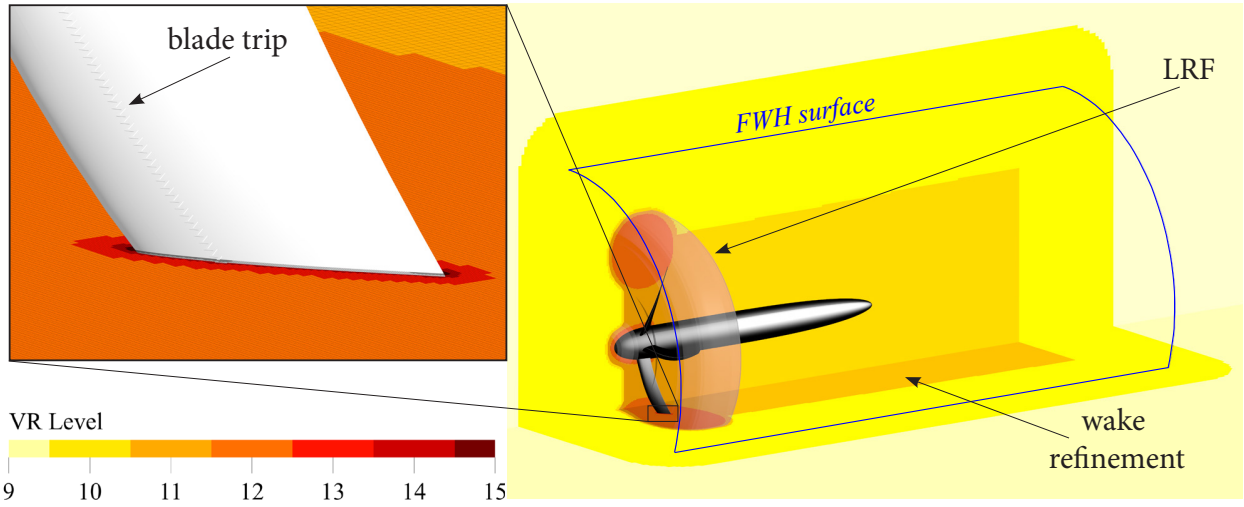


Figure 3: VR distribution and outline of the fixed FW-H surface.

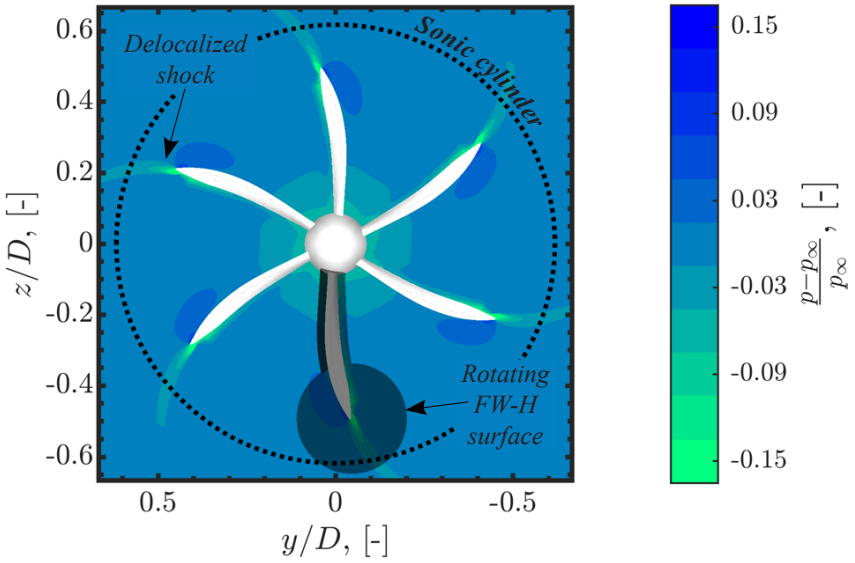


Figure 4: Pressure distribution in the rotor plane.

location. Finally, the time-domain pressure signal is examined to provide additional insight into waveform characteristics.

Figure 5 shows the normalized time derivative of pressure, $\frac{1}{\rho_0 c_0^2}, \partial p/\partial t$, which provides a measure of local flow dilatation and compression, and serves as a qualitative indicator of acoustic source regions and wave propagation. The left panel corresponds to the propeller frontal plane, while the right panel shows a transversal plane. From the frontal view, a spiral wave pattern radiating from the blade-tip region is observed, forming a helicoidal structure that extends into the far field, in agreement with the predictions reported by Chapman.[43] Looking at the contour plot in the transversal plane, the waves generated at the blade tips are observed to propagate predominantly in directions normal to the propeller axis, which is indicative of a dipolar radiation pattern. In addition, the mean flow velocity leads to inclined wavefronts due to the downstream convection of acoustic disturbances. The presence of locally irregular structures in the wake region highlights the contribution of hydrodynamic (pseudo-sound) fluctuations, which remain confined to the near field and do not contribute efficiently to far-field acoustic radiation.

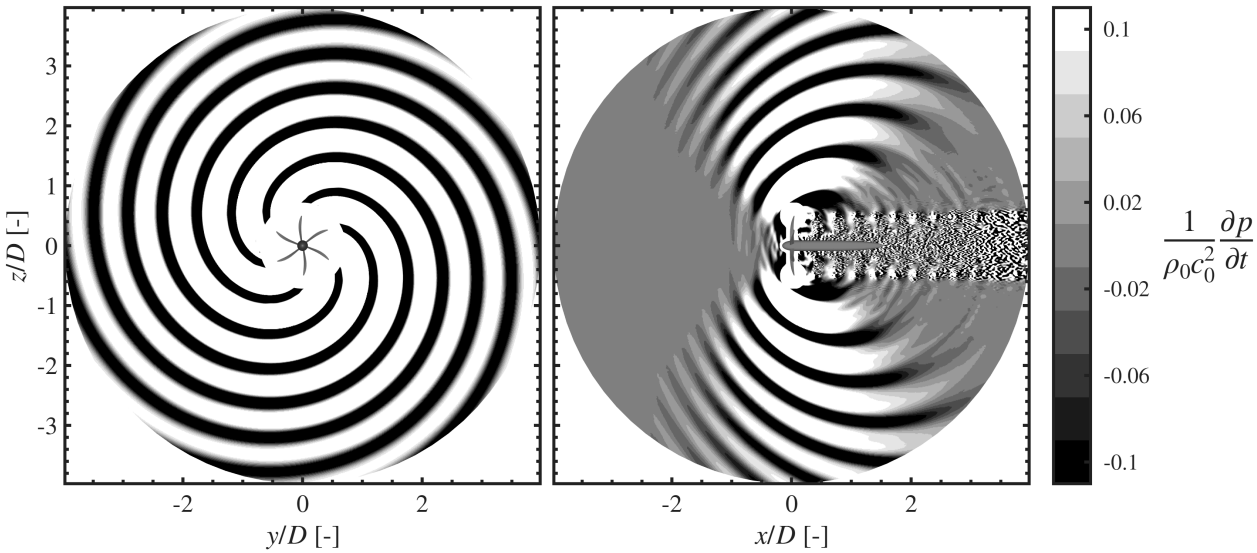


Figure 5: Dilatation field around the propeller obtained from direct CFD data.

Figure 6 shows the far-field directivity in the propeller transversal plane, computed using different formulations of the FW-H equation. Specifically, `SLD` denotes the solid formulation of Formulation 1A, `PRM` indicates the permeable formulation of Formulation 1A, and `PRM TRANSONIC` corresponds to the formulations described in Section II.B. Given the symmetry observed in the dilatation field with respect to positive and negative $z$, only the lower half of the directivity is reported. The angle is defined such that 0° corresponds to the downstream direction and 180° to the upstream direction. All formulations exhibit a clear dipolar radiation pattern, consistent with dilatation field observed before. The main differences are observed in the amplitude of the primary lobes. In particular, the solid formulation systematically underestimates the sound levels, which can be attributed to the absence of quadrupole (volume) contributions, which are important near the blade tips. The comparison between the classical permeable formulation and the de-singularized approach highlights additional differences. While both methods include volume effects implicitly, the classical permeable formulation relies on flow data sampled on a fixed surface located away from the body, where numerical dissipation have attenuated high-frequency fluctuations. This results in a reduced acoustic amplitude compared to the de-singularized formulation, which relies on a surface tightly coupled to the rotating blades.

Further insight is obtained by analysing the frequency spectra at a representative observer location. Figure 7 shows the sound pressure level spectra for a microphone located below the propeller, in the region corresponding to the lower directivity lobe. The frequency is normalized by the blade passing frequency (BPF). Comparing the solid and the de-singularized permeable formulations, a similar spectral structure is observed, with distinct tonal peaks at integer multiples of the BPF. However, the amplitude of these tones is consistently lower in the solid formulation, again reflecting the absence of quadrupole contributions. These volume sources are particularly important in transonic conditions, where strong velocity gradients and

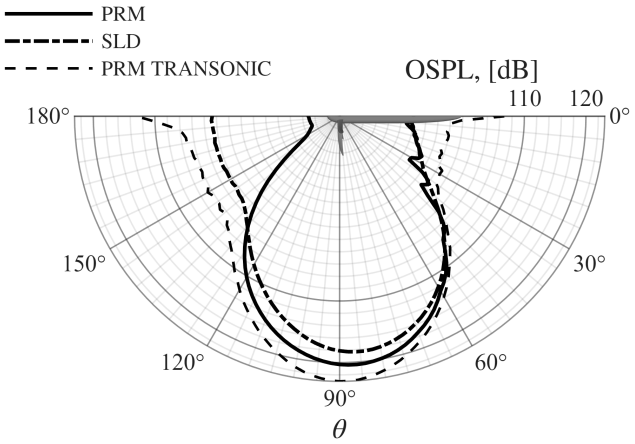


Figure 6: Overall Sound Pressure Level (OSPL) directivity plot computed with different FW-H formulations.

compressibility effects at the blade tips enhance high-frequency content. In contrast, the classical permeable formulation shows a progressive attenuation of the tonal peaks. While the first few harmonics are reasonably captured, a systematic reduction in amplitude is observed from approximately the third harmonic onwards, eventually leading to a near-complete loss of high-frequency content. This behaviour is not physical and is attributed to numerical dissipation in the input CFD data. In particular, the fixed FW-H surface is located in a region where the mesh is coarser and further from the primary noise sources, leading to additional attenuation of fluctuations. This effect is present in general for permeable formulations, but is further emphasized in the present case due to the increased numerical dissipation associated with the transonic LBM solver compared to its low-Mach counterpart.[37] As a consequence, the commonly used criterion of approximately 15 points per wavelength (in space and time) may no longer be sufficient to accurately resolve higher-frequency acoustic components. Although further mesh refinement could potentially mitigate this discrepancy, the finest simulation considered in this work already reaches nearly one billion cells, making additional refinement computationally prohibitive.

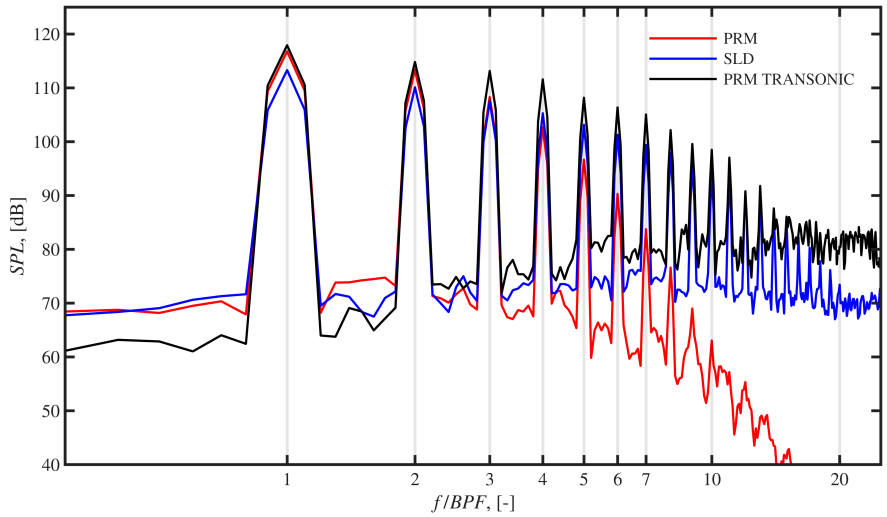


Figure 7: Sound pressure level spectra computed with different FW-H formulations at a microphone located 15 m below the propeller.

To complement the spectral analysis, it is also important to examine the acoustic signal in the time domain, as this provides additional information on waveform shape, phase, and steepness that cannot be fully inferred from the frequency spectrum alone. Figure 8 shows the phase-conditional average pressure, $\langle p \,|\, \phi \rangle$, over one blade-passing period (BPP), obtained by averaging over ten rotor revolutions. All formulations exhibit a similar overall waveform, characterized by a slight compression phase followed by a strong and rapid expansion associated with the passage of the blade-tip acoustic wave. After the expansion phase, the pressure

recovers to its initial level in all formulations, completing the acoustic cycle over one blade-passing period. The compression phase, occurring up to approximately $t/BPP \approx 0.4$, shows comparable gradients across all formulations. Differences become evident during the expansion phase, where both amplitude and temporal extent vary. Specifically, the de-singularized formulation predicts the highest expansion peak and the sharpest waveform, consistent with the stronger high-frequency content observed in the spectra. In contrast, the solid formulation exhibits a reduced peak amplitude and the narrowest temporal extent of the expansion region, reflecting the absence of quadrupole contributions. The classical permeable formulation shows the lowest expansion peak distributed over the broadest temporal region, yielding a smoother waveform. This behaviour is indicative of numerical dissipation, which attenuates high-frequency components and spreads the signal over a longer time scale. Although phase-averaging reduces stochastic fluctuations, small oscillations remain visible in the de-singularized signal. These can be further reduced by increasing the time-step ratio $\sigma$ (see Section II.B), which effectively increases temporal filtering during the FW-H integration. However, increasing $\sigma$ also increases the cost of the post-processing stage, both in terms of computational time and memory requirements. In the present work, a value of $\sigma = 10$ is adopted as a compromise between signal smoothness and computational efficiency.

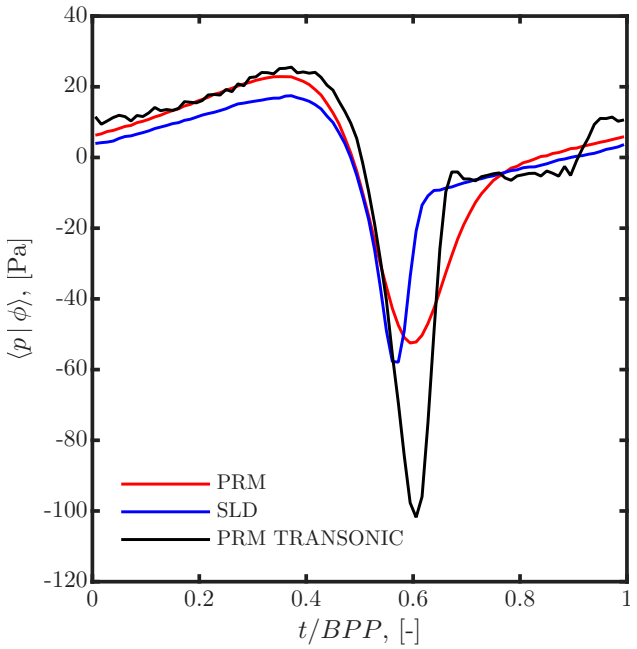


Figure 8: Phase-conditional average of pressure, $\langle p \,|\, \phi \rangle$, during one blade-passing period (BPP) computed with different FW-H formulations at a microphone located 15 m below the propeller.

## VI. Conclusion

In this work, the robustness of a permeable-surface transonic FW–H formulation has been investigated for the aeroacoustic prediction of a propeller operating in transonic conditions. The analysis focused on assessing the ability of a de-singularized strategy, based on Formulations 1-DS and 1A-DS by Casalino,[18] to provide consistent far-field noise predictions in the presence of strong compressibility effects. This assessment is carried out through a systematic comparison with classical FW–H formulations.

Prior the comparison, the inspection of the dilatation field from CFD data confirmed that the dominant acoustic sources are located in the blade-tip region, where compressibility effects generate coherent wave structures that propagate predominantly normal to the propeller axis. This behaviour is consistent with a dipolar radiation pattern and highlights the importance of accurately resolving the flow in regions of strong gradients.

The comparison of FW–H formulations showed that the solid formulation systematically underestimates acoustic levels due to the absence of quadrupole contributions, which are relevant in the present transonic regime. The classical permeable formulation, although accounting for volume effects, exhibits a significant

attenuation of high-frequency content, which is attributed to numerical dissipation and spatial filtering of the CFD data when the integration surface is placed away from the source region.

In contrast, the de-singularized formulation provides a more robust and consistent prediction of both amplitude and spectral content, preserving high-frequency components and yielding sharper time-domain waveforms. This improved performance is achieved by enabling the use of integration surfaces tightly fitted to the blade geometry, allowing quadrupole effects in the vicinity of the blade tip to be captured without relying on propagation through dissipative regions of the CFD domain.

A practical aspect of the formulation concerns the choice of the time-step ratio $\sigma$, which controls the temporal resolution of the FW–H integration. As discussed, $\sigma$ introduces an effective low-pass filtering of the signal and must be selected consistently with the target maximum frequency of interest. In particular, the condition $\Delta t = \sigma \Delta t_{\mathrm{CFD}} \leq 1/(N_{\mathrm{Nyq}} f_{\max})$ should be satisfied to avoid aliasing. In this framework, values of $\sigma \approx 8$–$10$ provide a suitable compromise between signal smoothness and spectral accuracy, provided that the CFD time step is chosen accordingly. This guideline offers a practical reference for setting up the post-processing in similar applications.

# Appendix

## .A. Grid Convergence Analysis

This section presents a grid convergence analysis addressing both steady aerodynamic forces and far-field acoustic predictions.

Figure 9 shows the variation of the time-averaged propeller thrust and torque coefficients with grid refinement. Three meshes with identical voxel-resolution (VR) distribution (see Section IV) but different absolute voxel sizes are considered. The coefficients are non-dimensionalized using $q_{ref_{prop}} = \rho n^2 D^2$, $S_{ref_{prop}} = D^2$, and $l_{ref_{prop}} = D$. The main characteristics of the three grids are summarized in Table 1. The results indicate that the *medium* grid provides aerodynamic predictions already converged with respect to the *fine* grid.

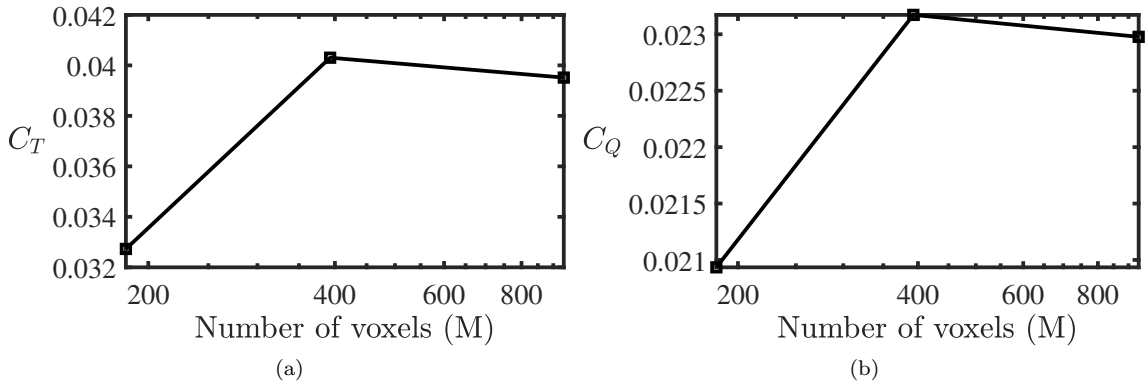


Figure 9: Thrust (a) and torque(b) coefficients for different number of voxels.

Table 1: Comparison of aerodynamic coefficients ($C_T$ and $C_Q$) for different mesh resolutions. Each row represents a level of grid refinement (Coarse, Medium, Fine), with the corresponding normalized grid spacing $\frac{\Delta x}{\Delta x_{\mathrm{fine}}}$, time step $\Delta t/T$, and number of voxels in millions.

| | $\frac{\Delta x}{\Delta x_{fine}}$ | $\Delta t/T$ | Voxels (M) | $C_T$ | $C_Q$ |
|---|---|---|---|---|---|
| *Coarse* | 2 | 1.897e-06 | 184.05 | 0.0327 | 0.0209 |
| *Medium* | $\sqrt{2}$ | 1.340e-06 | 392.96 | 0.0403 | 0.0232 |
| *Fine* | 1 | 9.483e-07 | 935.96 | 0.00395 | 0.0230 |

The effect of grid refinement on acoustic predictions is shown in Fig. 10, which reports the sound pressure level (SPL) spectra at a reference microphone located 15 m ($\approx 3$ propeller diameters) below the propeller in the $xz$ plane. Results are presented for the solid formulation (a), the permeable formulation (b), and direct

noise computation from CFD data (c). For the solid formulation, convergence of the tonal components is observed already on the coarse grid, although some differences remain in the broadband content. In contrast, the permeable formulation exhibits a stronger sensitivity to grid resolution, particularly at higher frequencies. As the integration surface is located away from the blade, numerical dissipation in the flow field leads to attenuation of high-frequency fluctuations. This results in a mesh-dependent reduction of the effective cut-off frequency, as clearly observed in Fig. 10-(b), where higher harmonics are progressively recovered with grid refinement. Finally, the direct computation of acoustic spectra from CFD data (Fig. 10-(c)) shows that only the first few harmonics are resolved, with higher-frequency content being strongly damped. This confirms that direct noise extraction is not suitable in the present transonic configuration and is therefore not considered in the remainder of the analysis. Although further mesh refinement could improve the resolution of high-frequency acoustic components for permeable formulations, the present results indicate that near-field quantities and solid FW–H predictions are already well converged. For permeable formulations, the remaining discrepancies at higher frequencies are attributed to numerical dissipation in the flow field, which is more pronounced for the transonic LBM solver compared to its low-Mach counterpart,[37] and to the location of the integration surface away from the primary noise sources.

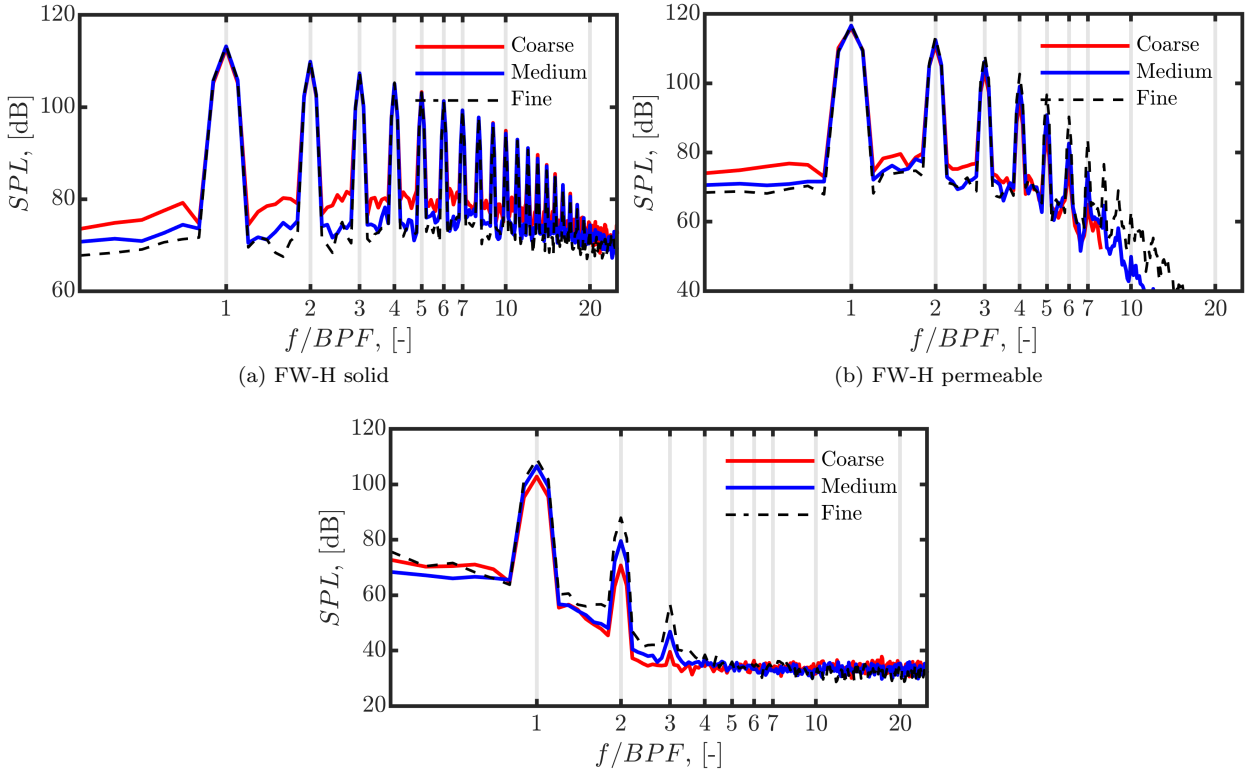


(a) FW-H solid

(b) FW-H permeable

(c) Direct probe

Figure 10: Pressure spectra at a microphone located 15 m below the propeller for three different mesh resolutions.

While additional refinement could mitigate these effects, the finest grid considered in this study already approaches one billion cells, making further refinement computationally prohibitive. Therefore, the fine grid is retained as a compromise between accuracy and computational cost, providing sufficiently resolved acoustic predictions for the purposes of the present analysis.

## References

[1]Van Zante, D. E., "Reestablishing Open Rotor as an Option for Significant Fuel Burn Improvements," *49th AIAA Aerospace Sciences Meeting including the New Horizons Forum and Aerospace Exposition*, American Institute of Aeronautics and Astronautics, AIAA, January 2011.

[2]Farassat, F., "Theory of Noise Generation from Moving Bodies with an Application to Helicopter Rotors," *NASA*

*Technical Report R-451*, 1975.

[3]Sticchi, E., Ragni, D., Casalino, D., and Avallone, F., "Aeroacoustic Installation Effects on a Propeller-Driven Strut-Braced Wing Aircraft," *Journal of Aircraft*, Vol. 0, No. 0, 0, pp. 1–21.

[4]Lighthill, M. J., "On Sound Generated Aerodynamically: 1. General Theory," *Proceeding of The Royal Society of London A*, Vol. A211, No. 1107, 1952, pp. 564–578.

[5]Curle, N., "The Influence of Solid Boundaries upon Aerodynamic Sound," *Proceeding of The Royal Society of London A*, Vol. A231, 1955, pp. 505–514.

[6]Ffowcs Williams, J. E. and Hawkings, D. L., "Sound Generated by Turbulence and Surfaces in Arbitrary Motion," *Philosophical Transactions of the Royal Society of London, Series A*, Vol. A264, No. 1151, 1969, pp. 321–342.

[7]Farassat, F., "Derivation of Formulations 1 and 1A of Farassat," *NASA/TM-2007-214853*, 2007.

[8]Brentner, K. S. and Farassat, F., "Modeling Aerodynamically Generated Sound of Helicopter Rotors," *Progress in Aerospace Sciences*, Vol. 39, No. 2–3, 2003, pp. 83–120.

[9]Ianniello, S., "Quadrupole Noise Predictions through the Ffowcs Williams–Hawkings Equation," *AIAA Journal*, Vol. 37, No. 10, 1999, pp. 1241–1247.

[10]Di Francescantonio, P., "A New Boundary Integral Formulation for the Prediction of Sound Radiation," *Journal of Sound and Vibration*, Vol. 202, No. 4, 1997, pp. 491–509.

[11]Morgans, A. S., Karabasov, S. A., Dowling, A. P., and Hynes, T. P., "Transonic Helicopter Noise," *AIAA Journal*, Vol. 43, No. 7, 2005, pp. 1512–1524.

[12]Ianniello, S., "New Perspectives in the Use of the Ffowcs Williams–Hawkings Equation for Aeroacoustic Analysis of Rotating Blades," *Journal of Fluid Mechanics*, Vol. 570, 2007, pp. 79–127.

[13]Brentner, K. S., "An Efficient and Robust Method for Predicting Helicopter Rotor High-Speed Impulsive Noise," *AIAA Journal*, Vol. 35, No. 3, 1997, pp. 438–444.

[14]Farassat, F. and Brentner, K. S., "Supersonic Quadrupole Noise Theory for High-Speed Helicopter Rotors," *Journal of Sound and Vibration*, Vol. 218, No. 3, 1998, pp. 481–500.

[15]Prieur, J. and Rahier, G., "Aeroacoustic integral methods, formulation and efficient numerical implementation," *Aerospace Science and Technology*, Vol. 5, No. 7, 2001, pp. 457–468.

[16]Delrieux, Y., Prieur, J., Rahier, G., and Drousie, G., "A New Implementation of Aeroacoustic Integral Method for Supersonic Deformable Control Surfaces," *9th AIAA/CEAS Aeroacoustics Conference and Exhibit*, May 2003.

[17]Rahier, G., "Comparison of surface and volume integral methods for transonic propeller acoustic predictions," *Computers & Fluids*, Vol. 179, 2019, pp. 178–193.

[18]Casalino, D., "Solution of the Ffowcs Williams–Hawkings equation for subsonic and supersonic permeable surfaces," *Journal of Sound and Vibration*, 2026, accepted for publication.

[19]Farassat, F., "Introduction to Generalized Functions with Applications in Aerodynamics and Aeroacoustics," *NASA Technical Paper 3428*, 1994.

[20]Ikeda, T., Enomoto, S., Yamamoto, K., and Amemiya, K., "Quadrupole Corrections for the Permeable-Surface Ffowcs Williams-Hawkings Equation," *AIAA Journal*, Vol. 55, No. 7, 2017, pp. 2307–2320.

[21]Mao, Y. and Hu, Z., "Analysis of Spurious Sound due to Vortical Flow through Permeable Surfaces," *Aerospace Science and Technology*, Vol. 96, 2020, pp. 105544.

[22]Casalino, D., "Mitigation of Truncation Effects in Spectral Ffowcs-Williams and Hawkings Analogy," *AIAA paper 2024-3366*, 2024.

[23]Farassat, F. and Succi, G. P., "A Review of Propeller Discrete Frequency Noise Prediction Technology with Emphasis on Two Current Methods for Time Domain Calculations," *Journal of Sound and Vibration*, Vol. 71, No. 3, 1980, pp. 399–419.

[24]Casalino, D., "An Advanced Time Approach for Acoustic Analogy Predictions," *Journal of Sound and Vibration*, Vol. 261, No. 4, 2003, pp. 583–612.

[25]Sticchi, E., Ragni, D., Casalino, D., and Avallone, F., "Aerodynamic Noise Prediction of Strut-Braced Wing Aircraft," *AIAA paper 2024-3012*, 2024.

[26]Marié, S., Ricot, D., and Sagaut, P., "Comparison between Lattice Boltzmann Method and Navier-Stokes High Order Schemes for Computational Aeroacoustics," *Journal of Computational Physics*, Vol. 228, 2009, pp. 1056–1070.

[27]Di Verniere, F., Sticchi, E., Casalino, D., Ragni, D., and Zamponi, R., "Aeroacoustic Analysis of a Transitioning Vectored-Thrust/Tilt-Rotor UAM Vehicle Using the LB/VLES Method," *European Rotorcraft Forum 2025*, 2025.

[28]Romani, G., Ye, Q., Avallone, F., Ragni, D., and Casalino, D., "Numerical analysis of fan noise for the NOVA boundary-layer ingestion configuration," *Aerospace Science and Technology*, Vol. 96, 2020, pp. 105532.

[29]Romani, G. and Casalino, D., "Rotorcraft Blade-Vortex Interaction Noise Prediction using the Lattice-Boltzmann Method," *Aerospace Science and Technology*, Vol. 800, 2019, pp. 147–157.

[30]Lockard, D., Humphreys, W., Khorrami, M., Fares, E., Casalino, D., and Ravetta, P., "Comparison of Computational and Experimental Microphone Array Results for an 18%-Scale Aircraft Model," *International Journal of Aeroacoustics*, Vol. 16, No. 4-5, 2017, pp. 358–381.

[31]Fares, E., Casalino, D., and Khorrami, M., "Evaluation of Airframe Noise Reduction Concepts via Simulations Using a Lattice Boltzmann Approach," *AIAA Paper 2015-2988*, 2015.

[32]Khorrami, M. R., Fares, E., and Casalino, D., "Towards Full Aircraft Airframe Noise Prediction: Lattice Boltzmann Simulations," *AIAA Paper 2014-2481*, June 2014.

[33]Avallone, F., Casalino, D., and Ragni, D., "Impingement of a Propeller Slipstream on a Leading Edge with a Flow-Permeable Insert: A Computational Aeroacoustic Study," *International Journal of Aeroacoustics*, Vol. 17, No. 6-8, 2018.

[34]Cerizza, D., Casalino, D., and Gonzalez-Martino, I., "An Extension of the Acoustics Evaluation of the NASA SDT Turbofan with Lattice-Boltzmann Methods," *AIAA Paper 2022-2886*, 2022.

[35]Casalino, D., Avallone, F., Gonzalez-Martino, I., and Ragni, D., "Aeroacoustic Study of a Wavy Stator Leading Edge in a Realistic Fan/OGV Stage," *ISROMAC 2017 (to appear on Journal of Sound and Vibration)*, 2017.

[36]Gonzalez-Martino, I. and Casalino, D., "Fan Tonal and Broadband Noise Simulations at Transonic Operating Conditions Using Lattice-Boltzmann Methods," *AIAA Paper 2018-3919*, 2018.

[37]Li, W., Wang, J., Gopalakrishnan, P., Li, Y., Zhang, R., and Chen, H., "Hybrid Lattice Boltzmann Approach for Simulation of High-Speed Flows," *AIAA Journal*, Vol. 61, No. 12, 2023, pp. 5548–5557.

[38]Chen, H., Zhang, R., and Gopalakrishnan, P., "Filtered lattice Boltzmann collision formulation enforcing isotropy and Galilean invariance," *Physica Scripta*, Vol. 95, No. 3, 2 2020.

[39]Teixeira, C. M., "Incorporating Turbulence Models into the Lattice-Boltzmann Method," *International Journal of Modern Physics C*, Vol. 9, 1998, pp. 1159–1175.

[40]Chen, H., Kandasamy, S., Orszag, S. A., Succi, S., and Yakhot, V., "Extended Boltzmann Kinetic Equation for Turbulent Flows," *Science*, Vol. 301, No. 5633, 2003, pp. 633–636.

[41]Chen, H., Orszag, S., Staroselsky, I., and Succi, S., "Expanded Analogy Between Boltzmann Kinetic Theory of Fluid and Turbulence," *Journal of Fluid Mechanics*, Vol. 519, Nov. 2004, pp. 301–314.

[42]Huang, Z., Siozos-Rousoulis, L., De Troyer, T., and Ghorbaniasl, G., "Helicopter rotor noise prediction using a convected FW-H equation in the frequency domain," *Applied Acoustics*, Vol. 140, 2018, pp. 122–131.

[43]Chapman, C. J., "The Structure of Rotating Sound Fields," *Proceedings: Mathematical and Physical Sciences*, Vol. 440, No. 1909, 1993, pp. 257–271.